Estimation of Pointing Errors of Large Radio Telescopes under Solar Radiation Based on Digital Twin

Shanxiang Wei , Deqing Kong * , Binlan Wang , Lianbo Fu , Wenrong Xiao , Zongming Yin , Yongxiang Li , Zhouzhou Xiao

Posted Date: 3 April 2024

doi: 10.20944/preprints202404.0306.v1

Keywords: digital twin; radio telescope; pointing error; solar radiation

 doi:10.20944/preprints202404.0306.v1

Article

Estimation of Pointing Errors of Large Radio Telescopes under Solar Radiation Based on Digital Twin

Shanxiang Wei [1], Deqing Kong [2,3,*], Binlan Wang [1], Lianbo Fu [4], Wenrong Xiao [1], Zongming Yin [1], Yongxiang Li [1] and Zhouzhou Xiao [4]

[1] School of Mechanical Engineering, Guizhou University of Engineering Science, Bijie 551700, China; gzgc@163.com
[2] Key Laboratory of Lunar and Deep Space Exploration, National Astronomical Observatories, Chinese Academy of Sciences, Beijing 100101, China; lpdc@nao.cas.cn
[3] School of Astronomy and Space Science, University of Chinese Academy of Sciences, Beijing 100049, China; astro@ucas.ac.cn
[4] School of Physics and Electronics, Henan University, Kaifeng 475004, China; xbmsk@henu.edu.cn
* Correspondence: kdq@bao.ac.cn(K.D.)

Abstract: The pointing accuracy of large radio telescopes is affected by antenna structure errors, installation errors, servo errors, gravity, and varying environmental factors. It is hard to estimate the pointing error of radio telescopes under solar radiation via the traditional multi-parameter static pointing models, due to the time-varying characteristics of the dynamic pointing error. There is still no effective way to estimate the dynamic pointing error of large radio telescopes under solar radiation up to now. To estimate the dynamic pointing error of large radio telescopes under solar radiation, a new way based on digital twin(DT) is tried in this paper. The operational framework of the DT system of large radio telescopes is introduced first. Then, the Wuqing 70-m radio telescope(WRT70) is taken as the research object, the digital models of which are created. Finally, the reliability of the WRT70's DT system is verified and the dynamic pointing error of WRT70(staying at the position of the elevation angle of 90° and the azimuth angle of 180°) on two sunny days in different seasons is estimated by the created DT system. The research results show that the pointing error of large radio telescopes under solar radiation fluctuates greatly and the seasonal differences are very striking. The maximum elevation pointing error of WRT70 under solar radiation around the winter solstice is over 40 arcsec, which should never be ignored. The way is feasible to estimate the dynamic pointing error of large radio telescopes staying at a specific position under solar radiation via constructing a DT system in this paper, but it is not yet able to estimate effectively the dynamic pointing error of large radio telescopes being in action. It is expected to establish a dynamic pointing error model and calibrate the dynamic pointing errors of large radio telescopes being in action by DT technology in the future.

Keywords: digital twin; radio telescope; pointing error; solar radiation

1. Introduction

Radio telescope serves as the key equipment to receive and detect radio waves from the universe, which plays an important role in space communication, deep space exploration, radio astronomy, and other research fields. In order to better receive and detect radio signals from distant space, a new generation of radio telescopes is tending to develop larger diameters. So far, there are two fully steerable radio telescopes in the world with apertures up to 100 meters, namely the Effelsberg radio telescope[1] and the Green Bank telescope[2]. In addition, China is building a 110-m fully-steerable radio telescope in Qitai, Xinjiang Province[3], and a 120-m fully-steerable radio telescope in Jingdong, Yunnan Province[4].

The Wuqing 70-m radio telescope(WRT70) is a typical wheel-track fully-steerable radio telescope, which is shown in Figure 1. Theoretically, the fully steerable radio telescope can point to any direction in horizontal space by driving the antenna to rotate around the vertical azimuth axis and the horizontal elevation axis, separately. In fact, there is always a large deviation between the commanded direction and the actual direction of a large fully steerable radio telescope, due to the influence of structure errors, installation errors, servo errors, gravity, and varying environmental factors[5]. The deviation is

 doi:10.20944/preprints202404.0306.v1

defined as the pointing error of radio telescopes, which is usually required not to exceed 1/10 of the beam width (half power beam width, HPBW)[6]. The larger the aperture of radio telescopes is, the smaller the allowable pointing error is. Therefore, the excessive pointing error of a large fully steerable radio telescope must be estimated and calibrated effectively. Generally, the pointing error caused by the antenna's structure errors, installation errors, servo errors, and gravity is repeatable and static, which can be estimated and calibrated by the classic multi-parameter pointing model[7]. However, the dynamic pointing error caused by varying environmental factors(including solar radiation and wind disturbance) is unrepeatable and time-varying, so estimating and calibrating it becomes very difficult[8].

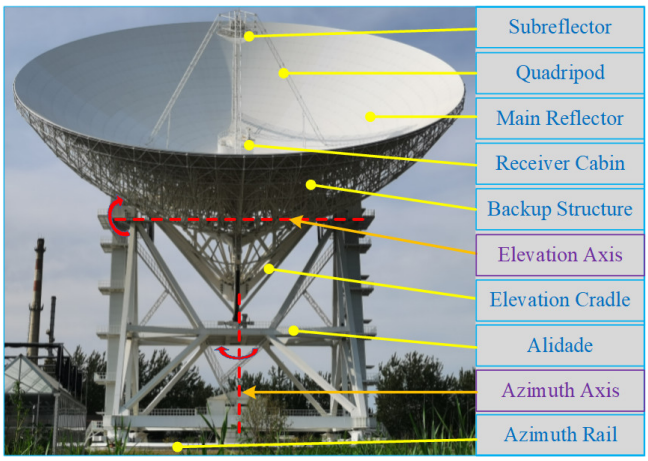

Figure 1. WRT70 radio telescope.

In order to estimate the dynamic pointing error, the thermal behaviors of radio telescopes under solar radiation have been discussed internationally. Over the past decades, the thermal behaviors of many foreign radio telescopes have been studied overseas via combining finite-element (FE) calculations and relative experiments, including the thermal deformation of the reflector system of the RT-70 radio telescope[9], the thermal design of the quadripod and backup structure of the IRAM 30-m telescope[10], and the thermal analysis of the alidade of the Medicina 32-m telescope and the Sardinia 64-m telescope[11–13]. In recent years, the thermal behaviors of several domestic radio telescopes also have been researched in China based on FE analysis and experimental measurements, such as the thermal effects of the alidade of the Nanshan 25-m radio telescope and the Miyun 50-m radio telescope[14,15], the nonuniform temperature and the thermal behavior of the Tianma 65-m radio telescope[16,17], the thermal deformations of the alidade and the reflector system of WRT70 [18,19]. To sum up, extensive studies on the thermal behaviors of radio telescopes have been done, but the research on estimating the total pointing error caused by the thermal behaviors of large radio telescopes is poor. There is still no effective way to estimate the dynamic pointing error of large radio telescopes under solar radiation up to now.

With the developments of new generation information technologies (New IT), digital twin (DT) has attracted researchers' attention and has been applied in the field of radio technology[20–22]. DT can create a digital model consistent with a physical device to simulate and predict the running state of the actual device[23]. In digital models, the behaviors and rules of a physical device can be represented by multidimensional models and multi-class parameters. Therefore, it will be very promising to use DT to predict the dynamic pointing error of large radio telescopes under solar radiation. In this paper, WRT70 is taken as the research object. Based on the DT system, the thermal behaviors of WRT70 under solar radiation can be presented in visual cloud images, and the dynamic pointing error caused by the thermal behaviors can be estimated via the rule model of pointing error. In Section 2, the operational framework of the DT system of large radio telescopes is introduced. In Section 3, the digital models of WRT70 are constructed, including the geometric model, physical model, behavior model, and rule

 doi:10.20944/preprints202404.0306.v1

model. In Section 4, the twin data of WRT70 is verified, and the pointing errors of WRT70 on two specific sunny days are estimated.

2. Operational Framework of the DT System of Large Radio Telescopes

According to the five-dimensional conceptual model of DT proposed by Professor F. Tao of Beihang University, the DT system of large radio telescopes consists of five parts, including physical telescope device, digital telescope model, twin data, service, and connection and interaction between units[24]. The operational framework of the DT system of large radio telescopes can be represented in Figure 2.

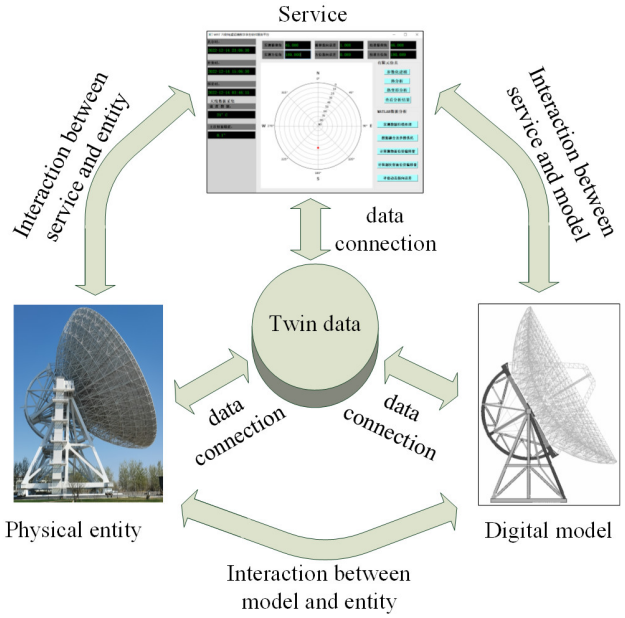

Figure 2. Operational framework of DT system of large radio telescopes.

First, the local state data of large radio telescopes is collected in real-time via a series of sensors installed on the physical telescope device, and stored in the data center of the observation station. Meanwhile, the digital telescope models are created by computer software based on the sensors sensing data. Then the global state of the physical telescope device is simulated and calculated by the digital telescope models based on the service unit. In addition, the twin data generated by the digital telescope models can be verified by the sensors sensing data, and the digital telescope models can be optimized and updated when necessary. Finally, the behaviors and rules of the physical telescope device can be predicted by analyzing the twin data.

3. Creation of the Digital Models of WRT70

The core task of building a DT system is to create digital models. The creation of the digital models of WRT70 includes geometric modeling, physical modeling, behavior modeling, and rule modeling, which will be described in detail below.

3.1. Geometric Modeling

Geometric modeling refers to the process of constructing a three-dimensional model of one geometric entity inside the computer by CAD software. There are two common CAD modeling methods: the GUI manual modeling and the instruction parametric modeling. In order to facilitate the modification of the geometric model and improve the modeling efficiency, the instruction parametric modeling is adopted here. The antenna's structure of WRT70 can be divided roughly into five components: alidade structure, elevation cradle, backup structure, main reflector, subreflector, and quadripod. Based on the geometric size and matching feature data of each component, the three-

 doi:10.20944/preprints202404.0306.v1

dimensional geometric model of WRT70 is constructed as Figure 3. The alidade serves as the foundation of WRT70, which can move around the vertical azimuth axis on the azimuth rail. The elevation cradle and the above structures are supported by the alidade via two elevation bearings, which can rotate around the horizontal elevation axis as a whole.

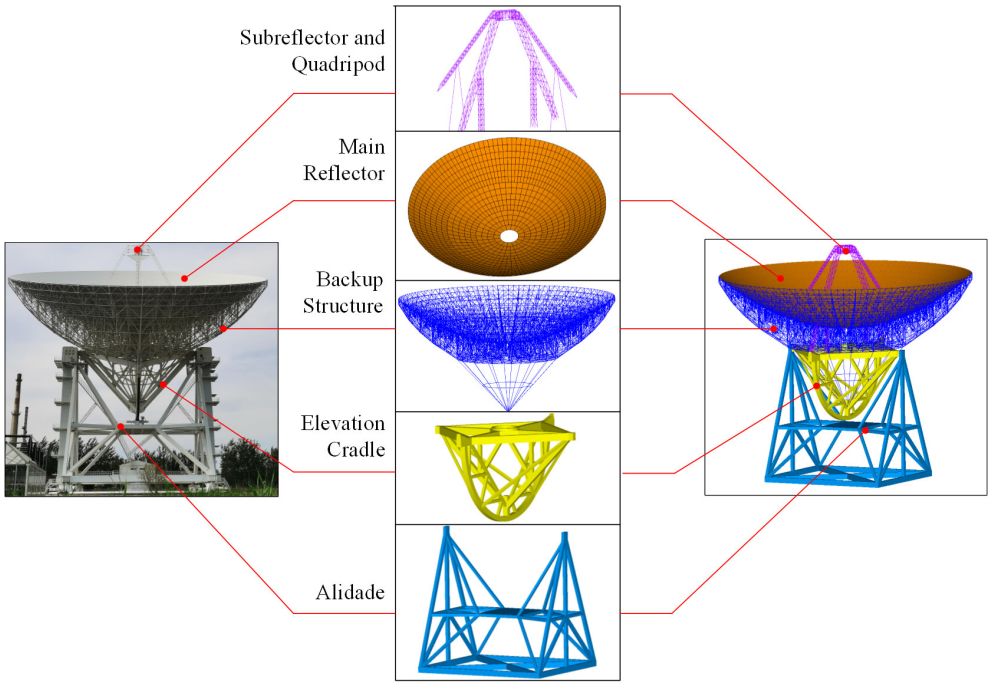

Figure 3. Geometric model of WRT70.

The alidade structure is a large spatial A-shaped truss, which is assembled by 52 rectangular beams with different cross-section sizes. The elevation cradle is composed of a diamond-cross truss, a half-big gear, and several diagonal-braced rectangular beams. The backup structure is a complex truss structure with circular symmetry, including an umbrella-support truss, a central main truss, 32 identical radial string beams, 320 ring string beams of different kinds, and hundreds of auxiliary round beams. The main reflector is a paraboloid with a diameter of 70 meters, which is composed of 1328 fan-shaped aluminum plates. The subreflector and quadripod include a hyperboloid-type subreflector with a diameter of 6 meters and a quadripod truss, where the subreflector is supported by the quadripod.

3.2. Physical Modeling

Physical modeling refers to the process of loading the boundary load data, measured by sensors from the physical telescope device, into the digital telescope model after equivalent transformation. Our team has installed various sensors on the physical structure of the WRT70 in past work, including 52 thermometers, 2 inclinometers, and 2 encoders. In addition, a weather station was installed around the physical entity of the WRT70 to monitor the environmental data such as atmospheric pressure, air temperature and humidity, solar radiation intensity, etc. The distribution of the above sensors on the WRT70 is shown in Figure 4, where unfortunately the left one of the two-dimentional inclinometers is broken now.

The reflector system(including backup structure, main reflector, subreflector, and quadripod) and the alidade structure of WRT70 are affected significantly by environmental factors. In order to facilitate the setting of boundary conditions and the loading of external loads, FE modeling is considered as the main way of physical modeling. The element number of the whole FE model of WRT70 is very huge so the periods of the FE modeling and simulation are extremely long. Due to the consideration of computer modeling and analysis speed, the reflector system and the alidade of WRT70 are physically

 doi:10.20944/preprints202404.0306.v1

modeled separately here. The FE models of the reflector system and the alidade and the marks of the applied boundary loads are shown in Figure 5. The temperature load is applied to the element nodes of the FE models in the form of surface convection heating and equivalent node temperature. The gravitational load is loaded onto the element nodes of the FE models in the form of gravitational acceleration. And the corresponding material properties of WRT70 are listed in Table 1.

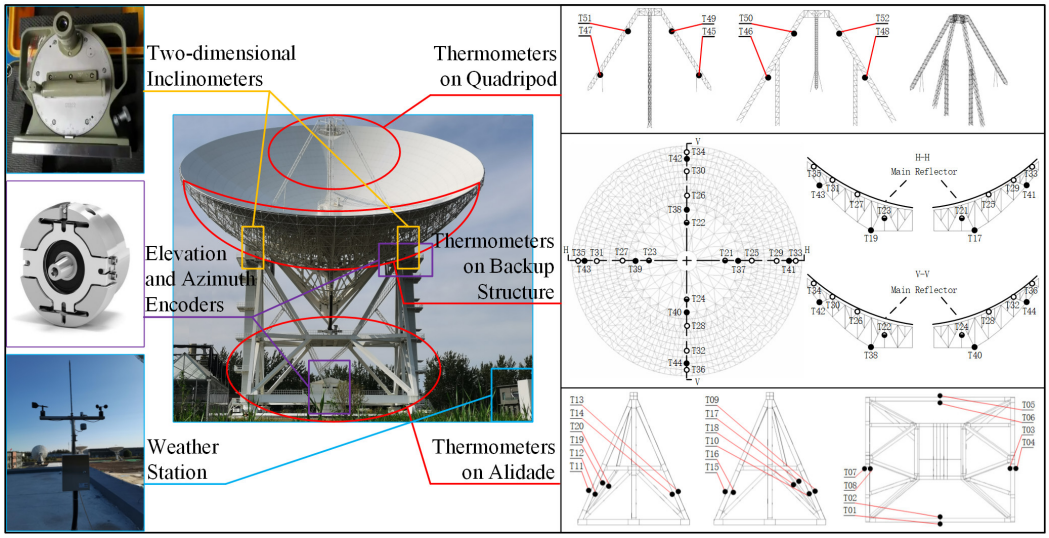

Figure 4. Distribution of temperature sensors on WRT70[18,19].

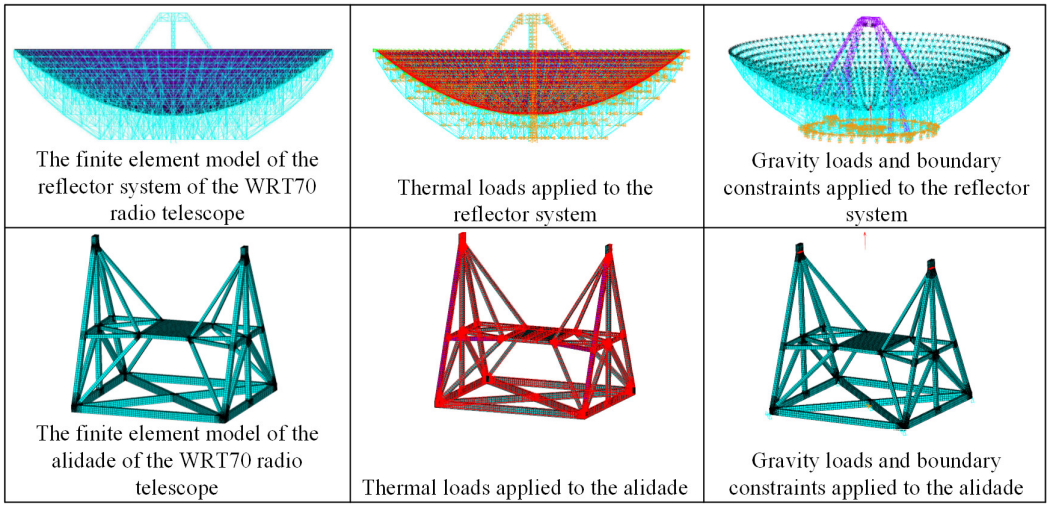

Figure 5. FE models and corresponding load marks of reflector system and alidade.

Table 1. Material properties of WRT70.

Component	Material	Density $kg\ m^{-3}$	Specific Heat $J\ kg^{-1}\ K^{-1}$	Thermal Conductivity $W\ m^{-1}\ K^{-1}$	Thermal Expansion $10^{-6}\ K^{-1}$
Main Reflector	Aluminum	2700	960	203	23.21
Backup, Quadripod, Alidade	Steel	7850	465	49.8	11.59

 doi:10.20944/preprints202404.0306.v1

3.3. Behavior Modeling

Behavior modeling refers to the process of obtaining the behavior characteristics of physical entity through digital simulation. Based on geometric modeling and physical modeling, the behavior characteristics of WRT70 can be obtained through FE simulation. The non-uniform temperature distributions and the corresponding thermal deformations of WRT70 under solar radiation can be visualized by contours, as shown in Figure 6 and 7.

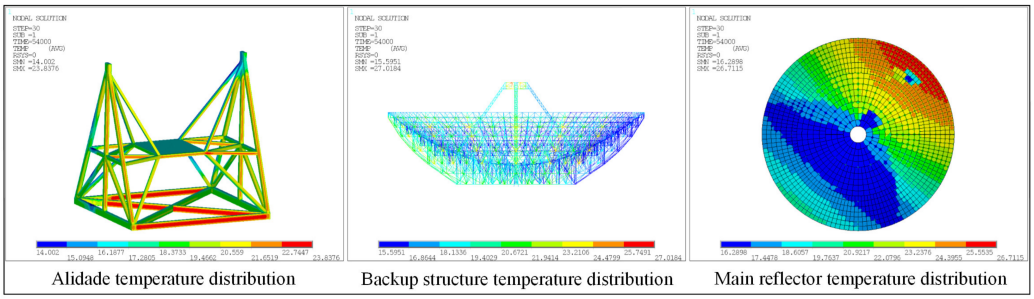

Figure 6. Temperature distribution contours of alidade and reflector system of WRT70.

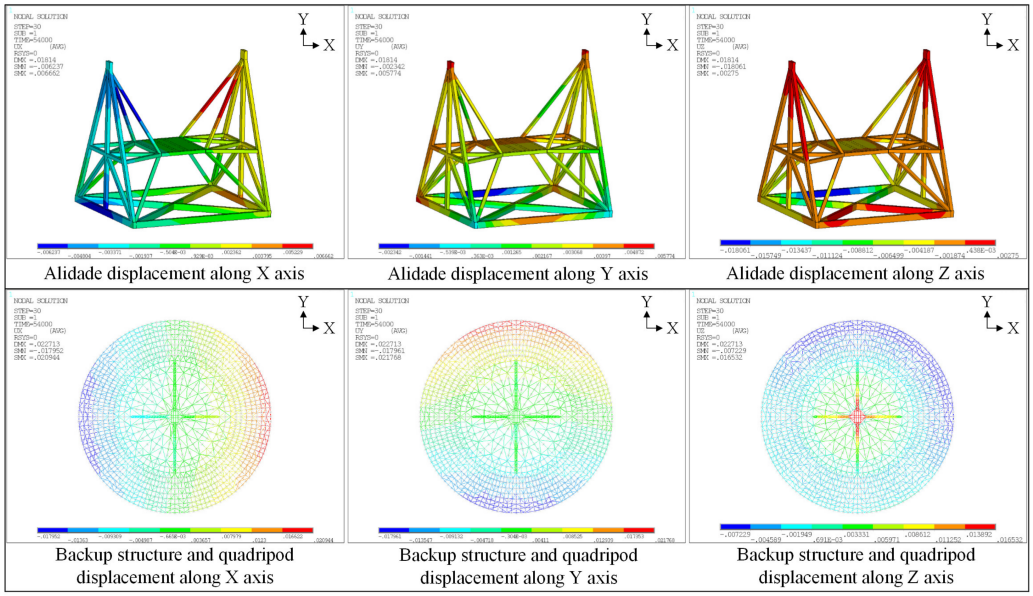

Figure 7. Thermal deformation contours of alidade and reflector system of WRT70.

3.4. Rule Modeling

Rule modeling refers to the process of obtaining the specific rules of the physical device through mathematical modeling and iterative calculation of the behavior characteristic data analyzed by the digital model. The dynamic rule of the pointing error of WRT70 under solar radiation is most desirable to be obtained in this paper. The pointing error of WRT70 is closely related to the tilt of the alidade and the pose variations of the reflector system, which is simply depicted in Figure 8. The tilt of the alidade can be simply calculated by combining the deformation displacement of several special nodes on the alidade, which will not be covered here. While the pose variations of the reflector system can only be solved by mathematical modeling and iterative calculation.

 doi:10.20944/preprints202404.0306.v1

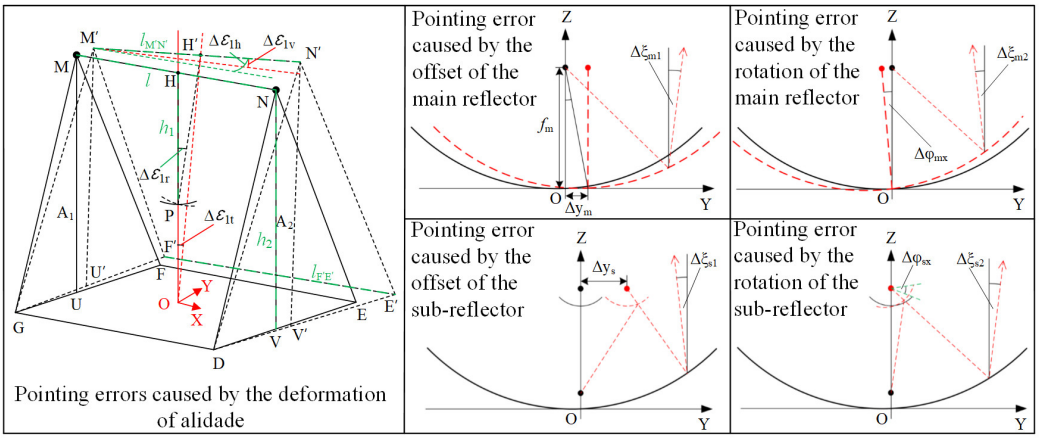

Figure 8. Depiction of pointing error caused by alidade deformation and pose variations of reflector system[18,19].

3.4.1. Pose Variation Rule of Reflector System

The pose variations of the main reflector need to be determined by solving the mathematical model of the best-fitting paraboloid of the deformed main reflector. The best-fitting paraboloid is a virtual paraboloid closest to the deformed main reflector, shown in Figure 9.

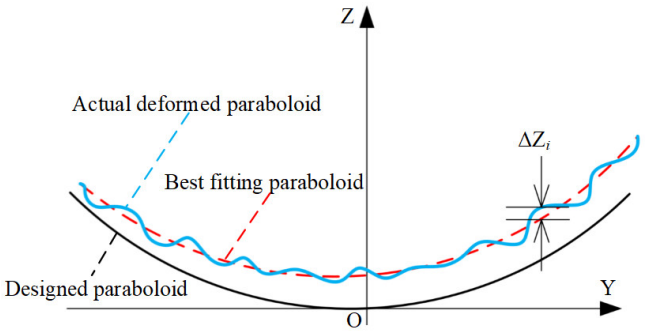

Figure 9. Best fitting paraboloid of main reflector[19].

The expression of the best fitting paraboloid is given as

$$z = \frac{x^2+y^2}{4f_{\mathrm{m}}} - \frac{x\Delta x_{\mathrm{m}}}{2f_{\mathrm{m}}} - \frac{y\Delta y_{\mathrm{m}}}{2f_{\mathrm{m}}} + \Delta z_{\mathrm{m}} + y\Delta\phi_{\mathrm{mx}} - x\Delta\phi_{\mathrm{my}} - \frac{x^2+y^2}{4f_{\mathrm{m}}}\frac{\Delta f_{\mathrm{m}}}{f_{\mathrm{m}}}, \tag{1}$$

where Δx_{m}, Δy_{m}, $\Delta z_{\mathrm{m}}$are the offsets of the best fitting paraboloid relative to the designed paraboloid along the X-axis, Y-axis, and Z axis, respectively. $\Delta\phi_{\mathrm{mx}}$ and $\Delta\phi_{\mathrm{my}}$ are the rotations of the best fitting paraboloid relative to the designed paraboloid at the apex around the X axis and Y axis, respectively. Δf_{m} is the offset of the focal length of the best-fitting paraboloid relative to the focal length of the designed paraboloid. The relationship between the above six key parameters and the displacement of each node on the main reflector could be expressed as[25]

$$A_{4\times6}\cdot\chi = B_{4\times1}, \tag{2}$$

where

$$A_{4\times6} = \begin{bmatrix} \sum_{i=1}^{N}\frac{x_i^2}{2f_{\mathrm{m}}} & \sum_{i=1}^{N}\frac{x_iy_i}{2f_{\mathrm{m}}} & -\sum_{i=1}^{N}x_i & -\sum_{i=1}^{N}x_iy_i & \sum_{i=1}^{N}x_i^2 & \sum_{i=1}^{N}\frac{x_iz_i}{f_{\mathrm{m}}} \\ \sum_{i=1}^{N}\frac{x_iy_i}{2f_{\mathrm{m}}} & \sum_{i=1}^{N}\frac{y_i^2}{2f_{\mathrm{m}}} & -\sum_{i=1}^{N}y_i & -\sum_{i=1}^{N}y_i^2 & \sum_{i=1}^{N}x_iy_i & \sum_{i=1}^{N}\frac{y_iz_i}{f_{\mathrm{m}}} \\ \sum_{i=1}^{N}\frac{x_iz_i}{2f_{\mathrm{m}}} & \sum_{i=1}^{N}\frac{y_iz_i}{2f_{\mathrm{m}}} & -\sum_{i=1}^{N}z_i & -\sum_{i=1}^{N}y_iz_i & \sum_{i=1}^{N}x_iz_i & \sum_{i=1}^{N}\frac{z_i^2}{f_{\mathrm{m}}} \\ \sum_{i=1}^{N}\frac{x_i}{2f_{\mathrm{m}}} & \sum_{i=1}^{N}\frac{y_i}{2f_{\mathrm{m}}} & -N & -\sum_{i=1}^{N}y_i & \sum_{i=1}^{N}x_i & \sum_{i=1}^{N}\frac{z_i}{f_{\mathrm{m}}} \end{bmatrix}, \tag{3}$$

 doi:10.20944/preprints202404.0306.v1

$$\chi = \begin{bmatrix} \Delta x_{\mathrm{m}} & \Delta y_{\mathrm{m}} & \Delta z_{\mathrm{m}} & \Delta \phi_{\mathrm{mx}} & \Delta \phi_{\mathrm{my}} & \Delta f_{\mathrm{m}} \end{bmatrix}^T, \tag{4}$$

$$B_{4\times 1} = \begin{bmatrix} \sum_{i=1}^{N} x_i(z_i - z_i') & \sum_{i=1}^{N} y_i(z_i - z_i') & \sum_{i=1}^{N} z_i(z_i - z_i') & \sum_{i=1}^{N} (z_i - z_i') \end{bmatrix}^T. \tag{5}$$

According to Equation 2, the pose variations of the main reflector, including Δx_{m}, Δy_{m}, Δz_{m}, $\Delta \phi_{\mathrm{mx}}$, and $\Delta \phi_{\mathrm{my}}$, could be determined.

The subreflector of WRT70 is fixed to the top of the quadripod. The pose variations of the subreflector can be almost equivalent to the ones of the top of the quadripod. There are four key nodes on the top structure of the quadripod, shown in Figure 7. Based on the displacement of the key nodes 1 to 4, the pose variations of the subreflector could be equivalently converted. The offsets Δx_{s}, Δy_{s} and Δz_{s} of the actual subreflector relative to the designed subreflector along X axis, Y axis, and Z axis could be expressed as Equation 6 to Equation 8, respectively[19]. The rotations $\Delta \phi_{\mathrm{sx}}$ and $\Delta \phi_{\mathrm{sx}}$ of the actual subreflector relative to the designed subreflector at the focus around X axis and Y axis could be expressed as Equation 9 and Equation 10, respectively[19]. (Δx_1, Δy_1, Δz_1), (Δx_2, Δy_2, Δz_2), (Δx_3, Δy_3, Δz_3) and (Δx_4, Δy_4, Δz_4) are the displacement of the key nodes 1 to 4, respectively.

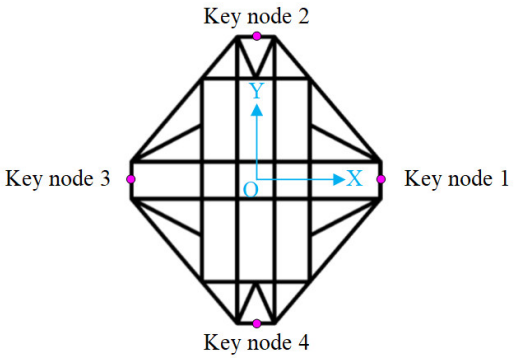

Figure 10. Key nodes on the top structure of quadripod[19].

$$\Delta x_{\mathrm{s}} = (\Delta x_1 + \Delta x_2 + \Delta x_3 + \Delta x_4/4, \tag{6}$$

$$\Delta y_{\mathrm{s}} = (\Delta y_1 + \Delta y_2 + \Delta y_3 + \Delta y_4/4, \tag{7}$$

$$\Delta z_{\mathrm{s}} = (\Delta z_1 + \Delta z_2 + \Delta z_3 + \Delta z_4 +)/4, \tag{8}$$

$$\Delta \phi_{\mathrm{sx}} = \arctan[(\Delta z_2 - \Delta z_4)/y_{24}], \tag{9}$$

$$\Delta \phi_{\mathrm{sy}} = \arctan[(\Delta z_3 - \Delta z_1)/x_{13}], \tag{10}$$

3.4.2. Pointing Error Rule of WRT70

The pointing error of radio telescopes can be subdivided into elevation pointing error, horizontal cross-elevation pointing error, and vertical cross-elevation pointing error. According to the geometric relationship of the alidade shown in Figure 8, the elevation pointing error $\Delta \xi_{1\mathrm{r}}$ caused by the rotation of the elevation cradle can be expressed as[26]

$$\Delta \xi_{1\mathrm{r}} = [(y_{\mathrm{N}} + y_{\mathrm{M}})/2 - y_{\mathrm{P}}]/h_1, \tag{11}$$

the elevation pointing error $\Delta \xi_{1\mathrm{t}}$ caused by the tilt deformation of the alidade can be expressed as[26]

$$\Delta \xi_{1\mathrm{e}} = [(y_{\mathrm{M}} - y_{\mathrm{U}}) + (y_{\mathrm{N}} - y_{\mathrm{V}}) -]/2h_2, \tag{12}$$

 doi:10.20944/preprints202404.0306.v1

the horizontal cross-elevation pointing error $\Delta\xi_{1h}$ caused by the alidade deformation can be expressed as[26]

$$\Delta\xi_{1h} = (y_M - y_N)/l_{M'N'} + (y_F - y_E)/l_{F'E'}, \tag{13}$$

the vertical cross-elevation pointing error $\Delta\xi_{1v}$ caused by the alidade deformation can be expressed as[26]

$$\Delta\xi_{1v} = (z_N - z_M)/l_{M'N'}, \tag{14}$$

where y_M and z_M are the displacements of A_1-tower top point M along the Y-axis and the Z-axis, respectively. y_N and z_N are the displacements of A_2-tower top point N along the Y-axis and the Z-axis, respectively. y_P is the Y-axis displacement of point P. h_1 is the distance between the horizontal elevation axis and the elevation driver. h_2 is the height of the horizontal elevation axis from the azimuth rail. And l is the width of the alidade. In particular, the elevation pointing error $\Delta\xi_{1r}$ caused by the rotation of elevation cradle and the elevation pointing error $\Delta\xi_{1t}$ caused by the tilt deformation of alidade can be merged into the total elevation pointing error $\Delta\xi_{1e}$ of alidade due to the consistent pointing direction of both.

In order to estimate the pointing error caused by the pose variations of the reflector system of radio telescopes, the concept of beam deviation factor (BDF) was first proposed by Ruze in 1965. BDF is defined as the ratio of the beam deviation of radio telescopes to the focal-line deviation of the parabolic reflector. The expression of BDF could be given as[27]

$$\mathrm{BDF} = \frac{48}{1+2\tau}\frac{f^2}{D^2}\left[1 - \frac{32f^2}{D^2}(\tau-1) + \tau\right] + \frac{32f^2}{D^2}\left\{-1 + \frac{16f^2}{D^2}(\tau-1)\left[-\ln\frac{f^2}{D^2} + \ln\left(\frac{1}{16} + \frac{f^2}{D^2}\right)\right]\right\}, \tag{15}$$

where D is the diameter of the main reflector or subreflector, f is the focal length of the primary focal or Cassegrain focal, and τ is the taper parameter.

Based on BDF and geometric optical path of reflector system, the elevation pointing error $\Delta\xi_{2e}$ caused by the pose variations($\Delta y_m, \Delta y_s, \varphi_{mx}, \varphi_{sx}$) of the reflector system can be expressed as[27]

$$\Delta\xi_{2e} = -\mathrm{BDF_m}\frac{\Delta y_m}{f_m} + (1+\mathrm{BDF_m})\Delta\varphi_{mx} + \left(\mathrm{BDF_m} - \frac{\mathrm{BDF_s}}{M}\right)\frac{\Delta y_s}{f_m} - \frac{\mathrm{BDF_s}}{M}\frac{2c}{f_m}\varphi_{sx}, \tag{16}$$

the horizontal cross-elevation pointing error $\Delta\xi_{2h}$ caused by the pose variations($\Delta x_m, \Delta x_s, \varphi_{my}, \varphi_{sy}$) of the reflector system can be expressed as[27]

$$\Delta\xi_{2h} = \left[-\mathrm{BDF_m}\frac{\Delta x_m}{f_m} + (1+\mathrm{BDF_m})\Delta\varphi_{my} + \left(\mathrm{BDF_m} - \frac{\mathrm{BDF_s}}{M}\right)\frac{\Delta x_s}{f_m} - \frac{\mathrm{BDF_s}}{M}\frac{2c}{f_m}\varphi_{sy}\right]\cos EL, \tag{17}$$

the vertical cross-elevation pointing error $\Delta\xi_{2v}$ caused by the pose variations($\Delta x_m, \Delta x_s, \varphi_{my}, \varphi_{sy}$) of the reflector system can be expressed as[27]

$$\Delta\xi_{2v} = \left[-\mathrm{BDF_m}\frac{\Delta x_m}{f_m} + (1+\mathrm{BDF_m})\Delta\varphi_{my} + \left(\mathrm{BDF_m} - \frac{\mathrm{BDF_s}}{M}\right)\frac{\Delta x_s}{f_m} - \frac{\mathrm{BDF_s}}{M}\frac{2c}{f_m}\varphi_{sy}\right]\sin EL, \tag{18}$$

where M is equivalent to $(c+a)/(c-a)$, a is the half of the real axis length of the hyperbolic subreflector, c is the half of the focal length of the hyperbolic subreflector, f_m is the focal length of the parabolic reflector, and EL is the elevation angle of WRT70.

Affected by varying environmental factors, the deformation of the alidade and reflector system WRT70 is the most significant. Ignoring the influence of azimuth rail and elevation cradle, the sum of the pointing errors caused by the deformation of the alidade and reflector system can be taken as the total pointing error of WRT70. Combining Equation 11 to 14 and Equation 16 to 18, the total elevation pointing error $\Delta\xi_e$ of WRT70 can be expressed as

$$\Delta\xi_e = \Delta\xi_{1e} + \Delta\xi_{2e}, \tag{19}$$

 doi:10.20944/preprints202404.0306.v1

the total horizontal cross-elevation pointing error $\Delta\xi_h$ of WRT70 can be expressed as

$$\Delta\xi_h = \Delta\xi_{1h} + \Delta\xi_{2h}, \tag{20}$$

the total vertical cross-elevation pointing error $\Delta\xi_v$ of WRT70 can be expressed as

$$\Delta\xi_v = \Delta\xi_{1v} + \Delta\xi_{2v}. \tag{21}$$

4. Verification of Structural Temperature Data and Estimation of Pointing Error for WRT70 under Solar Radiation

Based on the DT system created above, the pointing error of WRT70 (keeping at the position of the elevation angle of 90° and the azimuth angle of 180°) on two specific sunny days(February 27, 2021, and June 5, 2021) is estimated in this paper. To verify the reliability of the above DT system, the structural temperature data and the pointing error data caused by the alidade deformation of the WRT70 are verifed below.

4.1. Verification of Structural Temperature Data

The distribution of the 52 temperature sensors on WRT70 is shown in Figure 4, with 20 temperature sensors(T01 to T20) on alidade, 24 temperature sensors(T21 to T44) on backup structure, and 8 temperature sensors(T45 to T52) on quadripod. The simulated temperature data and the measured temperature data for several representative locations(T01, T03, T05 on alidade, and T49, T51, T52 on backup structure) on February 27, 2021, and June 5, 2021 are compared respectively in Figure 11 and 12.

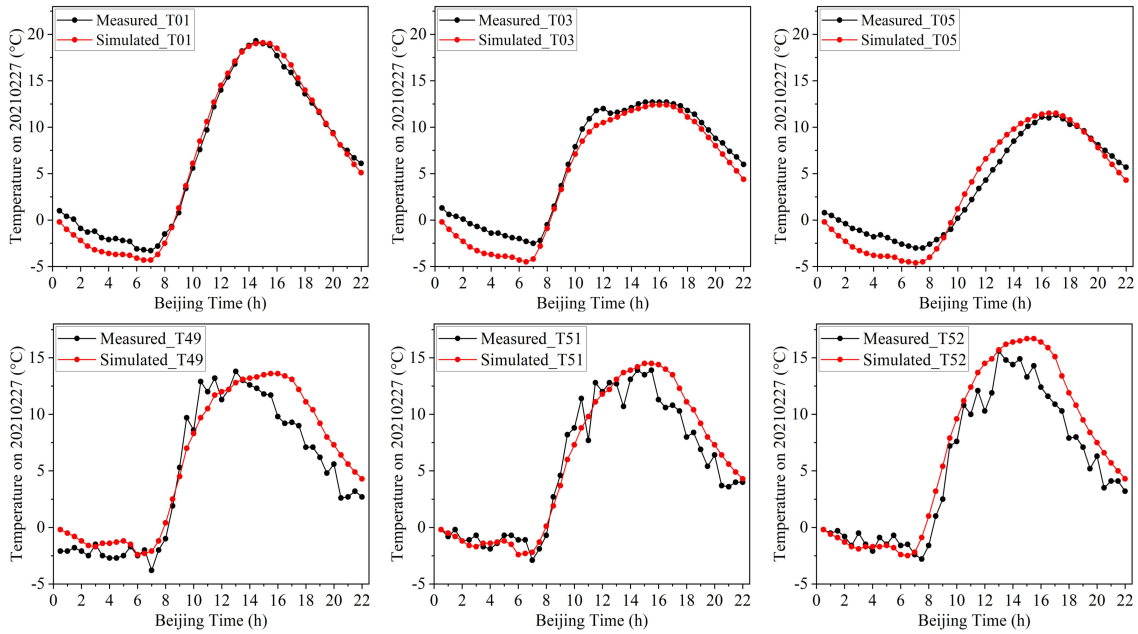

Figure 11. Comparison between measured temperature and simulated temperature for several representative locations(T01, T03, T05, T49, T51, T52) of WRT70 on February 27, 2021.

 doi:10.20944/preprints202404.0306.v1

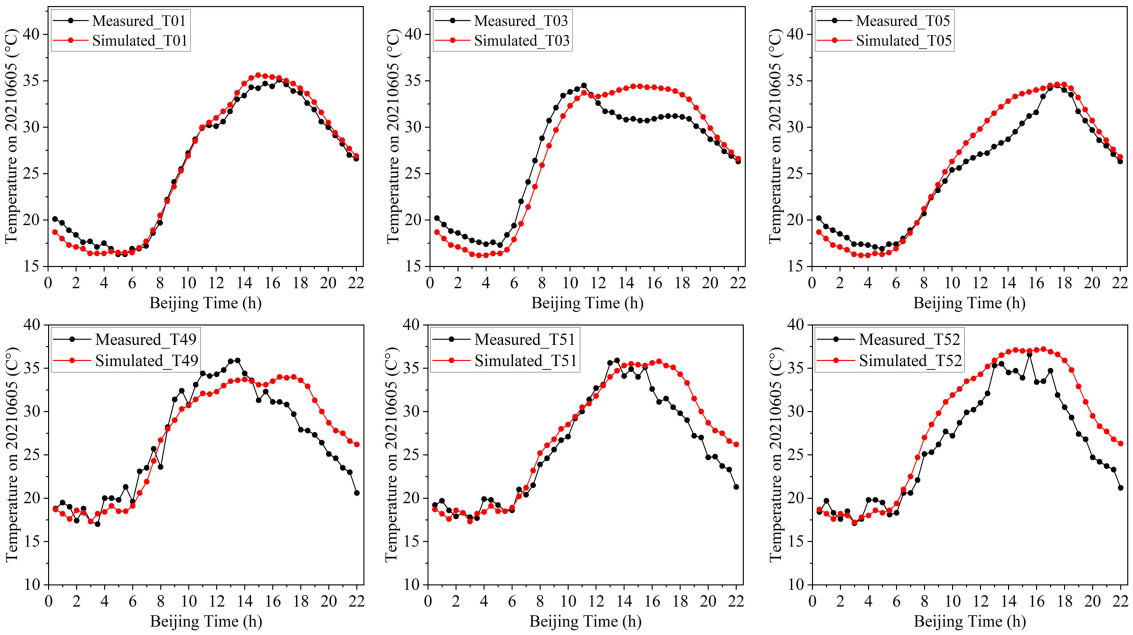

Figure 12. Comparison between measured temperature and simulated temperature for several representative locations(T01, T03, T05, T49, T51, T52) of WRT70 on June 5, 2021.

The comparison results in Figure 11 and 12 show that the simulated temperature data and the measured temperature data at several representative locations of the alidade and backup structure are in good agreement. The temperature difference at different locations of the WRT70 on February 27, 2021 is larger than that on June 5, 2021.

4.2. Verification of Pointing Error Data Caused by Alidade Deformation

The pointing error caused by alidade deformation can be subdivided into four subitems($\Delta\xi_{1r}$, $\Delta\xi_{1t}$, $\Delta\xi_{1h}$, and $\Delta\xi_{1v}$) to calculate according to Equation 11 to 14. Meanwhile, the elevation pointing error $\Delta\xi_{1r}$ caused by the rotation of elevation cradle and the horizontal cross-elevation pointing error $\Delta\xi_{1h}$ caused by alidade deformation can be measured by elevation and azimuth encoders, and the elevation pointing error $\Delta\xi_{1t}$ caused by the tilt deformation of alidade and the vertical cross-elevation pointing error $\Delta\xi_{1v}$ caused by alidade deformation can be measured by two-dimensional inclinometers. The calculated data and the measured data for the four subitems of the pointing error caused by alidade deformation of the WRT70 on February 27, 2021, and June 5, 2021, are compared in Figure 13.

The comparison results in Figure 13 show that the calculated data and the measured data for the four subitems($\Delta\xi_{1r}$, $\Delta\xi_{1t}$, $\Delta\xi_{1h}$, and $\Delta\xi_{1v}$) of the pointing error caused by alidade deformation of the WRT70 are all in agreement to some degree. The fluctuation range of the elevation pointing error $\Delta\xi_{1r}$ caused by the rotation of the elevation cradle on February 27, 2021, is over 20 arcsec according to the calculated data and the measured data of the elevation encoder. The fluctuation range of the elevation pointing error $\Delta\xi_{1t}$ caused by the tilt deformation of the alidade on February 27, 2021, is close to 15 arcsec according to the calculated data and the measured data around the X axis of the two-dimensional inclinometer. The fluctuation range of the horizontal cross-elevation pointing error $\Delta\xi_{1h}$ caused by alidade deformation on June 5, 2021, is over 20 arcsec according to the calculated data and the measured data of the azimuth encoder. The fluctuation range of the vertical cross-elevation pointing error $\Delta\xi_{1v}$ caused by alidade deformation on June 5, 2021, is over 10 arcsec according to the calculated data and the measured data around the Y axis of the two-dimensional inclinometer.

 doi:10.20944/preprints202404.0306.v1

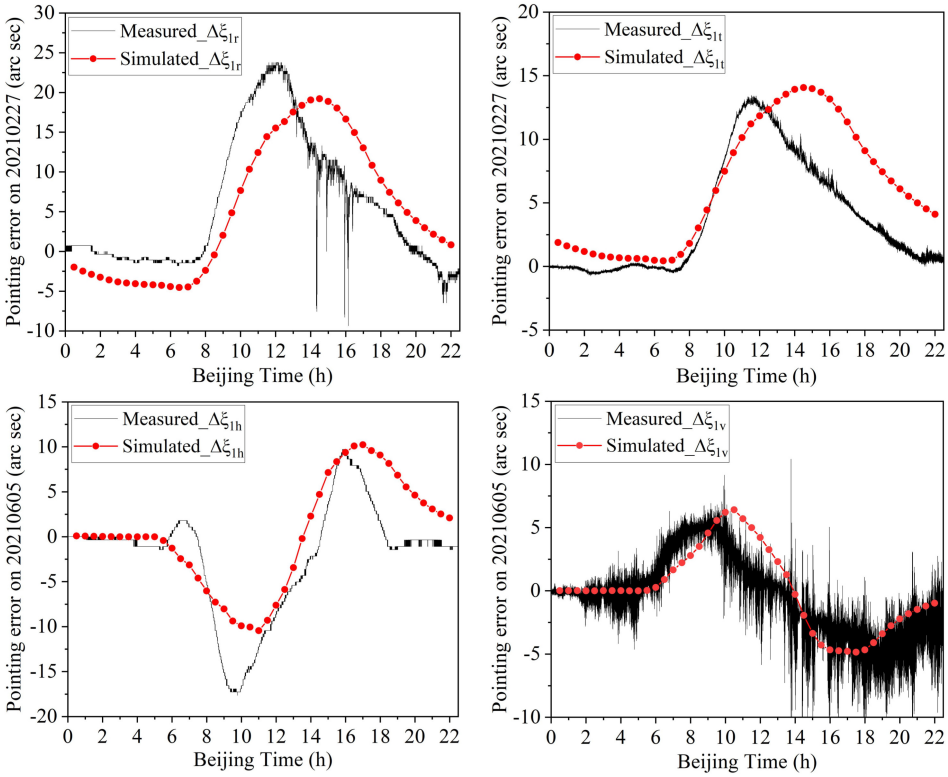

Figure 13. Comparison between calculated data and measured data for four subitems($\Delta\xi_{1r}$, $\Delta\xi_{1t}$, $\Delta\xi_{1h}$, and $\Delta\xi_{1v}$) of pointing error caused by alidade deformation of WRT70 on February 27, 2021, and June 5, 2021

4.3. Estimation of Total Pointing Error of WRT70

According to the rule model of the DT system established above, the total pointing errors of WRT70 under solar radiation can be calculated. Figure 14 depicts the estimated results of the total pointing error of WRT70 under solar radiation on February 27, 2021, and June 5, 2021.

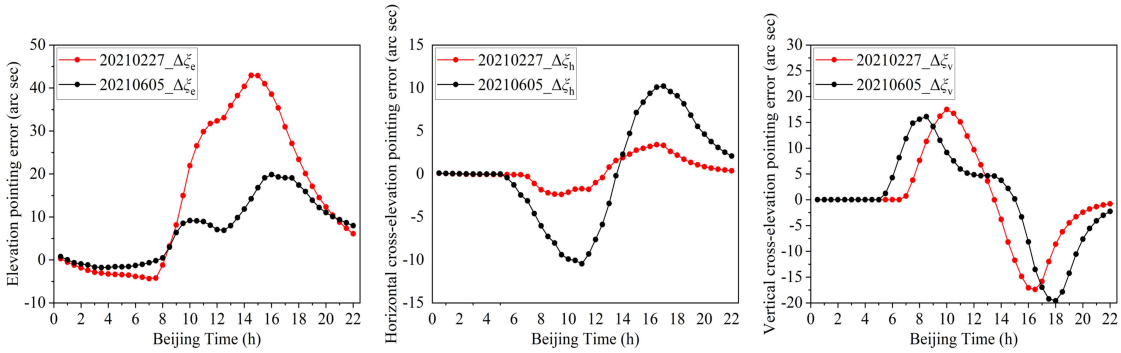

Figure 14. Pointing error of WRT70 on February 27, 2021, and June 5, 2021.

The above results show that the pointing error of WRT70 under solar radiation varies greatly and fluctuates sinusoidal, which should never be ignored. The elevation pointing error of WRT70 around the winter solstice is over 40 arcsec, which is much larger than that around the summer solstice. The horizontal cross-elevation pointing error of WRT70 around the winter solstice fluctuates little and much less than that around the summer solstice.

 doi:10.20944/preprints202404.0306.v1

5. Conclusion

In this paper, the DT system of a large radio telescope is constructed and the total pointing error of WRT70 under solar radiation is estimated. According to the research results, the following conclusions can be drawn.

(1) The DT system of WRT70 constructed in this paper is reliable to a great degree. The simulated temperature data and the measured temperature data at several representative locations of WRT70 are proved to be in good agreement. The calculated data and the measured data for the four subitems of the pointing error caused by alidade deformation of the WRT70 are all in agreement to some degree.

(2) The total pointing error of large radio telescopes(staying at a specific position) under solar radiation can be calculated by the DT system. The total pointing error of WRT70(staying at the position of the elevation angle of 90° and the azimuth angle of 180°) on February 27, 2021, and June 5, 2021, is estimated based on the DT system in this paper.

(3) The pointing error of large radio telescopes under solar radiation fluctuates greatly and the seasonal differences are very striking, which should never be ignored. The maximum elevation pointing error of WRT70 around the winter solstice is over 40 arcsec, which is much larger than that around the summer solstice.

This study provides a feasible way to estimate the dynamic pointing error of large radio telescopes staying at a specific position. Unfortunately, the way is not yet able to estimate effectively the dynamic pointing error of large radio telescopes being in action. However, it will be promising for establishing a dynamic pointing error model and calibrating the dynamic pointing errors of large radio telescopes(being in action) by DT technology in the future.

Author Contributions: Data curation, K.D. and F.L.; Methodology, W.S.; Writing—original draft preparation, W.S.; Writing—review and editing, W.S. and K.D.; Software W.B.; Investigation, W.B. and X.Z.; Supervision, X.W., Y.Z. and L.Y. All authors have read and agreed to the published version of the manuscript.

Funding: This research was funded by the National Natural Science Foundation of China(Grant No. 12303091), the Scientific and Technological Innovation Team of Higher Education Institutions under the Education Department of Guizhou of China(Grant No. QJJ[2023]093), the Natural Science Research Project of Education Department of Guizhou of China(Grant No. QJJ[2022]398), the Bijie City Science and Technology Project(Grant No. BKLH[2023]18), the Natural Science Research Project of Guizhou Higher Education Institutions of China (Grant No. QJJ[2023]047), and the Bijie City Science and Technology Project (Grant No. BKLH[2023]9).

Data Availability Statement: Data is unavailable.

Conflicts of Interest: The authors declare no conflicts of interest.

Abbreviations

The following abbreviations are used in this manuscript:

WTR70	Wuqing 70-m Radio Telescope
HPBW	Half Power Beam Width
FE	Finite Element
DT	Digital Twin
New IT	New generation Information Technologies

References

1. Wielebinski R.; Junkes N.; Grahl B. The effelsberg 100-m radio telescope: construction and forty years of radio astronomy. *Journal of Astronomical History and Heritage* **2011**, *14*, 3-21.
2. Hunter, T.; Schwab, F.; White, S.; Ford, J.; Ghigo, F.; Maddalena, R.; Mason, B.; Nelson, J.; Prestage, R.; Ray, J.; Ries, P.; Simon, R.; Srikanth, S.; Whiteis, P. Holographic Measurement and Improvement of the Green Bank Telescope Surface. *Publications of the Astronomical Society of the Pacific* **2011**, *123*, 1087.
3. Wang, N. Introduction for QTT Project. In Proceedings of 2019 URSI Asia-Pacific Radio Science Conference(AP-RASC), New Delhi, India, 09-15 March 2019.

 doi:10.20944/preprints202404.0306.v1

4. Wang, M.; Xu, Y.H.; Wang, J.C.; Li, D.W.; Wang, S.W.; Zhao, W.L.; Hao, L.F.; Cheng, X.M.; Dong, L.; He, G.X.; He, C.; Dai, W.; Li, Z.X.; Xu, C.; Yang, G.H.; Yang, F.H.; Gao, Y.F.; Gao, G.N.; Guo, S.J.; Chen, W.; Dong, J.; Huang, Y.X. Jingdong 120-m pulsar radio telescope. *Sci. China Phys. Mech. Astron.* **2022**, *52*, 119501.
5. Gawronski W. Control and pointing challenges of antennas and telescopes. In Proceedings of the American Control Conference, Portland, OR, USA, 08-10 June 2005; Volume 6.
6. Levy, R. *Structural Engineering of Microwave Antennas*, 1st ed.; IEEE Press: New York, NY, USA, 1996.
7. Yu, L.F.; Wang, J.Q.; Zhao, R.B.; Dong, J.; Zuo, X.T.; Gou, W.; Liu, Q.H.; Fan, Q.Y. The Establishment of Pointing Model for the TM65 m Radio Telescope. *Chinese Astronomy and Astrophysics* **2015**, *39*, 524-537.
8. Liang W.; Huang J.; Zhang J. Real-Time Estimation of Wind-Induced Pointing Error via Accelerations Measurement for Large Reflector Antenna. *IEEE Access* **2020**, *8*, 71812-71820.
9. Borovkov, A.; Shevchenko, D.V.; Gimmelman, V.G.; Machuev, Y.I.; Gaev, A. Finite-element modeling and thermal analysis of the RT-70 radio telescope main reflector. In Proceedings of 4th International Conference on Antenna Theory and Techniques, Sevastopol, Ukraine, 09-12 September 2003; Volume 2.
10. Greve, A.; Bremer, M.; Penalver, J.; Raffin, P.; Morris, D. Improvement of the IRAM 30-m telescope from temperature measurements and finite-element calculations. *IEEE Transactions on Antennas and Propagation* **2005**, *53*, 851-860.
11. Pisanu T.; Buffa, F.; Morsiani, M.; Pernechele, C.; Poppi, S. Thermal behavior of the Medicina 32 meter Radio Telescope. In Proceedings of SPIE - The International Society for Optical Engineering, San Diego, California, United States, 22 July 2010; Volume 7739.
12. Pisanu T.; Buffa, F.; Poppi, S.; Marongiu, P.; Serra, G.; Vargiu, G.; Concu, R. The SRT inclinometer for monitoring the rail and the thermal gradient effects on the alidade structure. In Proceedings of SPIE - The International Society for Optical Engineering, Montréal, Quebec, Canada, 22 July 2014; Volume 9145.
13. Attoli, A.; Stochino, F.; Buffa, F.; Poppi, S.; Serra, G.; Sanna, G.; Sanna, G. Sardinia Radio Telescope structural behavior under solar thermal load. *Structures* **2022**, *39*, 901-916.
14. Xu, Q.; Xue, F.; Wang, H.; Yi, L. Measurement and Correction of Pointing Error Caused by Radio Telescope Alidade Deformation based on Biaxial Inclination Sensor. *Micromachines* **2023**, *14*, 1283.
15. Kong, D.Q.; Jiang, Z.Y.; Zhang, H.B.; Wu, Y.X. Effects of sunshine temperature on axis angle measurement errors of large radio telescopes and the correction method. *Sci. Sin. Tech.* **2019**, *49*, 1331-1342.
16. Qian, H.L.; Chen, D.S.; Fan, F.; Liu, Y.; Shen, S.Z. Evaluation of solar temperature field under different wind speeds for Shanghai 65 m radio telescope. *International Journal of Steel Structures* **2016**, *16*, 383-393.
17. Fu, L.; Ling, Q.B.; Geng, X.G.; Wang, J.Q.; Jiang, Y.; Yu, L.F.; Zhang, Y. The alidade temperature behaviour of TM65m antenna and its effects on pointing accuracy. In Proceedings of SPIE - The International Society for Optical Engineering, Edinburgh, United Kingdom, 22 July 2016; Volume 9912.
18. Wei, S.X.; Kong, D.Q.; Wang, Q.M. Effect of the alidade thermal behavior on the pointing accuracy of a large radio telescope. *Research in Astronomy and Astrophysics* **2021**, *21*, 137.
19. Wei, S.X.; Kong, D.Q.; Wang, Q.M. Effect of the reflector system thermal behavior on the pointing accuracy of large radio telescopes. *Journal of Astronomical Telescopes, Instruments, and Systems* **2023**, *9*, 028002.
20. Bednarz, T.; Branchaud, D.; Wang, F.; Baker, J.; Marquarding, M. Digital Twin of the Australian Square Kilometre Array. In Proceedings of SIGGRAPH Asia 2020, New York, NY, United States, 04 - 13 December 2020
21. Li, Q.W.; Jiang, P.; li, H. Prognostics and health management of FAST cable-net structure based on digital twin technology. *Research in Astronomy and Astrophysics* **2020**, *20*, 067.
22. Wen, J.J.; Liu, Z.G.; Song, Y.F.; Meng, X.K.; Yao,J.H. Rapid Modeling Method for The Digital Twin of Five-hundred-meter Aperture Spherical Radio Telescope. *IAENG Internaitonal Journal of Computer Science* **2022**, *22*, 482-488.
23. Botín-Sanabria, D.M.; Mihaita, A.-S.; Peimbert-García, R.E.; Ramírez-Moreno, M.A.; Ramírez-Mendoza, R.A.; Lozoya-Santos, J.d.J. Digital Twin Technology Challenges and Applications: A Comprehensive Review. *Remote Sens* **2022**, *14*, 1335.
24. Tao, F.; Zhang, M.;Liu, Y.S.; Nee, A. Digital twin driven prognostics and health management for complex equipment. *CIRP Annals* **2018**, *67*, 1788.
25. Zhang, J.; Huang, J.;Wang, S.F.; Wang, C.S. An Active Pointing Compensator for Large Beam Waveguide Antenna Under Wind Disturbance. *IEEE/ASME Transactions on Mechatronics* **2015**, *21*, 860-871.

 doi:10.20944/preprints202404.0306.v1

26. Greve, A.; Bremer, M. *Thermal Design and Thermal Behaviour of Radio Telescopes and their Enclosures* , 1st ed.; Springer Press: Berlin Heidelberg, German, 2010.
27. Baars, J.W. *The Paraboloidal Reflector Antenna in Radio Astronomy and Communication*, 1st ed.; Springer Press: New York, USA, 2007.